ACS Catalysis

RESEARCH ARTICLE

pubs.acs.org/acscatalysis

Structural and Electrocatalytic Properties of PtIrCo/C Catalysts for Oxygen Reduction Reaction

Rameshwori Loukrakpam,[†] Bridgid N. Wanjala,[†] Jun Yin,[†] Bin Fang,[†] Jin Luo,[†] Minhua Shao,[*,‡] Lesia Protsailo,[‡] Tetsuo Kawamura,[§] Yongsheng Chen,[∥] Valeri Petkov,[⊥] and Chuan-Jian Zhong[*,†]

[†]Department of Chemistry, State University of New York at Binghamton, Binghamton, New York 13902, United States

[‡]UTC Power, 195 Governor's Highway, South Windsor, Connecticut 06074, United States

[§]Toyota Motor Engineering & Manufacturing North America Inc., 1588 Woodridge Ave., Ann Arbor, Michigan 48105, United States

[∥]EMS Energy Institute and Department of Energy and Mineral Engineering, Pennsylvania State University, University Park, Pennsylvania 16802, United States

[⊥]Department of Physics, Central Michigan University, Mt. Pleasant, Michigan 48859, United States

Supporting Information

ABSTRACT: This paper describes the results of an investigation of the synthesis of PtIrCo nanoparticles (2−3 nm) for electrocatalytic oxygen reduction reaction. The carbon-supported PtIrCo catalysts (PtIrCo/C) were thermally treated at temperatures ranging from 400 to 900 °C. The size, composition, and atomic-scale structures of the PtIrCo/C catalysts were characterized for establishing their correlation with the electrocatalytic activity toward oxygen reduction reaction. The specific activity was found to increase by a factor of 3−5 for the PtIrCo/C catalysts in comparison with Pt/C catalysts. A correlation was identified between the specific activity and the nanoparticle's fcc-type lattice parameter. The specific activity increases whereas the fcc-type lattice parameter decreases with the thermal treatment temperature. This correlation was further substantiated by analyzing the interatomic spatial parameters in the trimetallic nanoparticles based on X-ray absorption fine structure spectroscopic and high-energy XRD experiments. Implications of these findings, along with the durability of the catalysts, to the design of active electrocatalysts were also discussed.

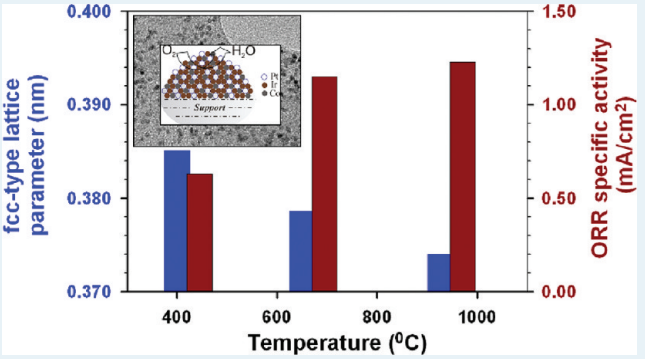

KEYWORDS: nanoengineered trimetallic catalysts, platinum-iridium-cobalt nanoparticles, oxygen reduction reaction, fcc-type lattice parameter, electrocatalytic activity and durability

INTRODUCTION

The study of Pt-based bimetallic and trimetallic catalysts (e.g., PtFe, PtAu, PtNi, PtCo, PtIr, PtVFe, PtNiFe, etc.) has been an important focal area of research and development of active, robust, and low cost catalysts for achieving the ultimate commercialization of fuel cells. The preparation of alloy catalysts has traditionally been based on methods such as coprecipitation, impregnation, sputtering, codeposition, electrodeposition, and so forth.[1−10] Molecularly engineered synthesis and processing strategies have recently been developed for the preparation of metal and alloy nanoparticle and supported catalysts.[11−15] One such method that has been utilized for the synthesis of controllable metal nanoparticles involved a combination of polyol reduction process and thermal decomposition of metal carbonyl compounds in the presence of a mixture of oleylamine and oleic acid as the capping agents.[11,12,16] For example, trimetallic platinum-vanadium-iron (PtVFe) and platinum-nickel-iron (PtNiFe) nanoparticles prepared by nanoengineered synthesis and processing methods were shown to exhibit excellent electrocatalytic activities for oxygen reduction reaction (ORR) in our earlier studies[12−15] and recently in polymer electrolyte membrane fuel cells (PEMFCs).[17,18] Much of the recent interest has focused on understanding of the electrocatalytic properties of alloy nanoparticle catalysts with different transition metals (e.g., PtCo for ORR[19,20]). Pt_3Co alloy catalysts have been demonstrated to exhibit significantly improved performance in electrocatalysis than Pt catalysts. The mass activity values of Pt_3Co/C catalysts have been reported to be between ~0.3 to 1.0 A/mg_{Pt} after current-resistance (IR) drop correction.[20,21] There are limited studies of Pt-based alloy electrocatalysts involving Ir as a second or third metal component. Considering the fact that Pt and Ir in the bulk phase forms stable alloy, which have been widely used in catalysis, casting, wielding, jewelry, and so forth, addition of iridium to the Pt−Co system is thus expected to

Received: January 16, 2011
Revised: March 29, 2011
Published: April 01, 2011

potentially increase the stability of the catalyst. For example, carbon-supported IrM (M = V, Mn, Fe, Co, and Ni) catalysts (7 to 16 nm) have been reported as anode catalysts in fuel cells.[22] PtIr electrocatalysts derived from composite nanotube materials have been reported to exhibit an increased electrocatalytic activity for methanol oxidation reaction.[23] Nanoporous PtIr bimetallic electrocatalysts prepared using hydrothermal methods were shown to exhibit high electroactive surface areas.[24] The presence of Ir was shown to significantly improve the electrocatalytic activity of Pt toward the electrochemical oxidation of methanol and oxygen reduction. The electrochemical performance of an unsupported $Pt_{85}Ir_{15}$ electrocatalyst was also evaluated as a bifunctional oxygen electrode in a unitized regenerative fuel cell (URFC).[25] The catalyst showed high oxygen evolution activity and ORR activity comparable to that for unsupported Pt black catalyst. In this type of fuel cell, the catalyst functions as the cathode in the fuel cell mode and as an oxygen evolution electrode in the electrolysis mode. Several electrocatalysts were prepared and tested in a single cell URFC system,[26,27] in which a significant performance improvement was observed as a result of the addition of Ir or IrO*x* to Pt black.

Pt-based trimetallic alloy electrocatalysts have received increasing interest in the design of advanced fuel cell catalysts by exploiting the synergistic lattice and electronic properties of such ternary systems.[12−15,17,18] Recently, the activity and stability of PtIrCo/C prepared by a carbothermal synthesis route for oxygen reduction have been studied by UTC.[28−30] The carbothermal process involved precipitation of metal salts onto preplatinized carbon and annealing at 926 °C to form alloys.[28] The specific activity of PtIrCo/C was shown to be ∼2 times higher than that of Pt/C. The surface area and activity losses of this catalyst were much less than those of Pt/C during potential cycling. Electrochemical surface areas of the PtIrX (X = Co, Ni, V) alloy catalysts with a particle size in the 2−5 nm range were also studied.[29,30]

Despite these prior studies of Ir-containing Pt alloy electrocatalysts prepared mostly by traditional preparation methods which have demonstrated interesting electrocatalytic activity, there have been limited reports of Ir-containing Pt alloy electrocatalysts with well-defined composition, size, and atomic-scale structural properties. Such structural properties have recently been shown to be important for a number of other bimetallic and trimetallic nanoparticle catalysts (e.g., PtCo, PtNi, PtNiCo, etc.) prepared by nanoengineered synthesis and processing methods.[31,32] There are several considerations for us to choose Ir as a component in the catalyst. In addition to those from studies on PtIr alloy electrocatalysts which were cited in our introduction section, the computational study by Ma and Balbuena[33] has suggested that incorporating Ir into the Pt-based alloys decreases the binding strength to OH, especially for Pt_2IrCo (111), and increases the tendency to resist dissolution in acidic media, which could lead to an enhanced stability of the catalyst. In this report, we report the results of an investigation of the structural and electrocatalytic properties of nanoengineered PtIrCo nanoparticles and carbon-supported PtIrCo catalysts for oxygen reduction reaction. The focus is the understanding of the effects of composition, size, and atomic structural properties on the electrocatalytic activity and stability.

EXPERIMENTAL SECTION

Chemicals. Platinum(II) acetylacetonate ($Pt(acac)_2$, 97% pure), Iridium carbonyl ($Ir_4(CO)_{12}$, 98% pure), Cobalt(II) acetylacetonate ($Co(acac)_2$, 97% pure), 1,2-hexadecanediol (90%), dioctyl ether (99%), oleyl amine (70%) and Nafion (5 wt %) were obtained from Aldrich. Oleic acid (99%) was obtained from Alfa Aesar and Carbon black from ECP, Ketjen Black International. All the other solvents were of analytical grade and were used without further purification.

Synthesis of PtIrCo Nanoparticles. The synthesis involved a modification of the methods reported previously for the synthesis of other trimetallic nanoparticles (e.g., PtVFe, PtNiFe, PtNiCo).[11,12,31,32] In an organic media, Pt (II) acetylacetonate and Cobalt(II) acetylacetonate were reduced with 1, 2-hexadecanediol, and Iridium carbonyl undergoes thermal decomposition in the presence of oleic acid and oleylamine as capping agents at a temperature of 270 °C. Synthesis of $Pt_{40}Ir_{28}Co_{32}$ is given as a typical example. 1.704 g of 1,2-hexadecanediol, 0.474 g of $Pt(acac)_2$, 0.249 g of $Ir_4(CO)_{12}$, 0.241 g of $Co(acac)_2$, 1.5 mL of oleylamine, and 1.5 mL of oleic acid were added to 180 mL of dioctyl ether solvent. The solution was purged with N_2 and was heated to 270 °C. The solution appeared dark brown color. After the reaction mixture was allowed to cool down to room temperature, the solution was transferred to a large flask under ambient environment. The black product was precipitated by adding ethanol. The complete precipitation was achieved either by overnight precipitation or by centrifugation. The yellow-brown supernatant was discarded. The nanoparticle product was dispersed and stored in hexane.

Preparation of Electrocatalysts. With the as-synthesized PtIrCo nanoparticles, the preparation involved the assembly on carbon support and the subsequent thermal processing (removal of capping monolayer and calcinations) of the PtIrCo/C catalysts. For the assembly of the as-synthesized PtIrCo nanoparticles on the carbon support materials (ECP, Ketjen Black International), 0.350 g of carbon black was suspended in 300 mL of hexane. The suspension was sonicated for 3 h. A 0.232 g portion of $Pt_{40}Ir_{28}Co_{32}$ was added into the suspension for an estimated 40% metal loading. The suspension was sonicated first for 1 h and followed by stirring for ∼16 h. The solvent of the suspension was evaporated by purging N_2. The powder was collected and dried under N_2.

The thermal processing of the PtIrCo/C catalysts followed our previously reported protocols with slight modifications.[12,13] Briefly, the catalyst was first heated to 260 °C in N_2 for 60 min; and then heated at 400 °C in 15% H_2 + 85% N_2 for 120 min.

Instrumentation and Measurements. Thermogravimetric Analysis (TGA), Transmission Electron Microscopy (TEM), High-Resolution Transmission Electron Microscopy-Energy Dispersive X-ray Spectroscopy (HRTEM-EDS), Direct Current Plasma-Atomic Emission Spectrometry (DCP-AES), Inductively Coupled Plasma-Optical Emission Spectroscopy (ICP-OES), X-ray Photoelectron Spectroscopy (XPS), X-ray powder diffraction (XRD), X-ray absorption fine structure (XAFS) spectroscopy, High energy X-ray Diffraction (HE-XRD) coupled to atomic pair distribution function (PDF) analysis, and electroananlytical techniques were used for the characterization of the nanoparticles and catalysts.

The composition was analyzed using the DCP-AES technique, which was performed on an ARL Fisons SS-7 Direct Current Plasma-Atomic Emission Spectrometer. The nanoparticle samples were dissolved in concentrated aqua regia, and then diluted to concentrations in the range of 1 to 50 ppm for analysis. Calibration curves were made from dissolved standards with concentrations from 0 to 50 ppm in the same acid matrix as the

unknowns. ICP-OES technique was also used for the composition analysis, which was performed using a Perkin-Elmer 2000 DV ICP-OES utilizing a cross-flow nebulizer with the following parameters: plasma 18.0 L $Ar_{(g)}$/min; auxiliary 0.3 L $Ar_{(g)}$/min; nebulizer 0.73 L $Ar_{(g)}$/min; power 1500 W; peristaltic pump rate 1.40 mL/min.

TGA was performed on a Perkin-Elmer Pyris 1-TGA for determining the concentration of nanoparticles in hexane suspension. The samples (~4 mg) were heated in a platinum pan.

TEM data were obtained on a Hitachi H-7000 electron microscope (100 kV). HRTEM- EDS data were obtained using a JEOL JEM 2010F at an acceleration voltage of 200 kV.

XRD data was collected from 20 to 90 degree 2θ with a step size of 0.5 at room temperature on a Phillips X′pert PW 3040 MPD diffractometer using Cu Kα λ = 1.5418 Å, equipped with a sealed Xe proportional detector and a diffracted beam graphite monochromator which filter out all but Kα radiation. The diffraction data was compared to the XRD database of International Centre for Diffraction Data (ICDD) (with a correction: 0.2 in 2θ value).

High-energy XRD measurements were performed at the beamline 11IDC, at the Advanced Photon Source, Argonne, using X-rays of energy 115 keV (λ = 0.1078 Å). The diffraction data were reduced to the so-called structure factors, $S(q)$, and then Fourier transformed to the corresponding atomic PDFs $G(r)$, using the relationship:

$$G(r) = \frac{2}{\pi}\int_{q=0}^{q_{max}} q[S(q) - 1]\sin(qr)\,dq \qquad (1)$$

where q_{max} = 25 $Å^{-1}$ in the present experiments. The wave vector q is defined as $q = 4\pi\sin(\theta)/\lambda$, where θ is half of the scattering angle and λ is the wavelength of the X-rays used. Note, as derived, atomic PDFs $G(r)$ are experimental quantities that oscillate around zero and show positive peaks at real space distances, r, where the local atomic density $\rho(r)$ exceeds the average one ρ_o. This behavior can be expressed by the equation $G(r) = 4\pi r\rho_o[\rho(r)/\rho_o - 1]$, which is the formal definition of the PDF $G(r)$. High-energy XRD and atomic PDFs have already proven to be very efficient in studying the atomic-scale structure of nanosized materials.[34,35]

Pt L3 edge (11,564 eV) and Co K edge (7,709 eV) X-ray absorption fine structure (XAFS) spectra were collected on the insertion device beamline of the Materials Research Collaborative Access Team (MRCAT) at the Advanced Photon Source, Argonne National Laboratory. All spectra were collected in transmission mode. A reference spectrum of Pt or Co foil for energy calibration was collected simultaneously with each scan using an additional ionization chamber. X-ray Absorption Near-edge Spectra (XANES) were processed using Athena.[36] EXAFS were extracted using Athena and fitting of EXAFS data was performed using Artemis.[36] Background removal and edge-step normalization were performed using the AUTOBK program.[36] FEFFIT[37] was then used to fit the EXAFS functions generated by the FEFF code (version 6.0).[38] The fitting was limited to a k range of 2.0−16.0 $Å^{-1}$ for Pt L3 edge spectrum, using a Hanning window with dk =1.0 $Å^{-1}$. The fits were performed to both the real and the imaginary parts of $\chi(R)$ in the region of $2.0 < R < 3.2$ Å. Details of the experimental setup and sample preparation are described elsewhere.[32]

Electrochemical measurements were performed using an EG&G 273 instrument. Glassy carbon (GC) electrodes (geometric area: 0.196 cm^2) were polished with 0.05 μm Al_2O_3 powders, followed by careful rinsing with deionized water. A typical suspension of the catalysts was prepared by suspending 5 mg catalysts in 4 mL of Millipore water with 20 μL of diluted Nafion solution (5 wt %). The suspension was ultrasonicated at 20% amplitude for 10 min and then quantitatively transferred to the surface of the polished GC disk. The experiments were performed in three-electrode electrochemical cells at room temperature. All experiments were done with 0.1 M $HClO_4$ (obtained from GFS chemicals) as electrolyte and was deaerated with high-purity nitrogen for cyclic voltametry (CV) and then saturated with oxygen for rotating disk electrode (RDE) measurements. The polarization curves were recorded after 50 potential cycles in the range of 0.02−1.2 V with a scanning rate of 100 mV/s in a N_2-saturated 0.1 M $HClO_4$ solution. The potentials are given with respect to the standard hydrogen electrode (RHE). In the square-wave potential cycling protocol for evaluating the durability of the catalysts, each cycle involved pulsing the potential to 0.65 for 5 s and to 1.2 V for 5 s. After every 5000 cycles, the ECA and ORR activity values were measured in a fresh N_2-saturated 0.1 M $HClO_4$ solution and a fresh O_2-saturated 0.1 M $HClO_4$ solution, respectively.

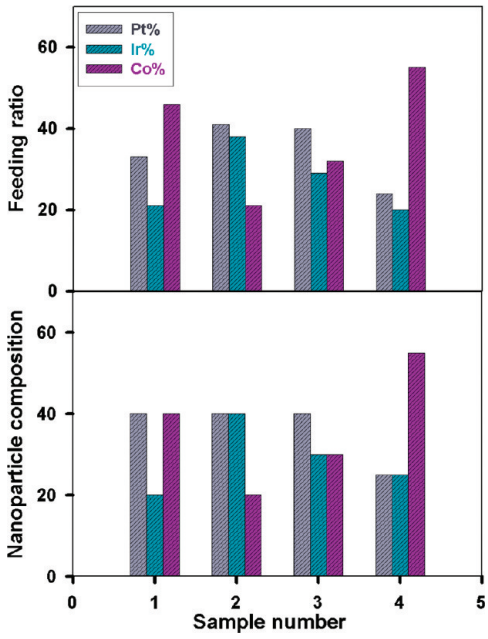

Figure 1. Correlation between the nanoparticle atomic composition (in % metal) and the feeding composition ratio of the metal precursors (in % metal) in the synthesis reaction.

RESULTS AND DISCUSSION

1. Size and Composition. *PtIrCo Nanoparticles.* The synthesis of PtIrCo nanoparticles involved the manipulation of several different parameters such as the reaction temperature, the feeding ratio of the metal precursors, the choice of metal precursors, and so forth. Pt (II) acetylacetonate and Co (II) acetylacetonate were reduced by 1, 2-hexadecanediol whereas Ir (0) carbonyl underwent thermal decomposition in the presence of oleic acid and oleylamine as capping agents. The formation of the nanoparticles was achieved in the organic media at a temperature of 270 °C. In Figure 1, the relative metal compositions in

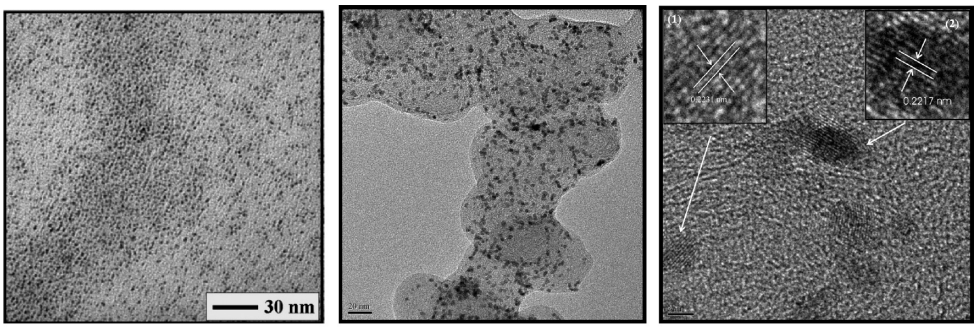

(A) (B) (C)

Figure 2. (A) TEM for a sample of as-synthesized $Pt_{25}Ir_{20}Co_{55}$ nanoparticles (2.2 ± 0.2 nm). (B) TEM (scale bar = 20 nm) and (C) HR-TEM (scale bar = 2 nm) for a sample of $Pt_{25}Ir_{20}Co_{55}/C$ catalyst treated at 400 °C. Inset: lattice fringes of (111) for the supported nanoparticles.

Table 1. Summary of the Morphological and fcc Lattice Parameters for Several PtIrCo/C Catalysts Treated at 400 °C

composition NPs	composition NPs/C	*M* (wt %)	size-1(TEM) (nm)[a]	size-2(TEM) (nm)[b]	size-3(XRD) (nm)[c]	lattice parameter (nm)
$Pt_{65}Ir_{11}Co_{24}$	$Pt_{59}Ir_{14}Co_{27}$	52	2.4 ± 0.2	3.6 ± 0.4	3.9	0.387
$Pt_{40}Ir_{28}Co_{32}$	$Pt_{37}Ir_{27}Co_{36}$	44	2.8 ± 0.2	4.4 ± 0.3	4.3	0.389
$Pt_{25}Ir_{20}Co_{55}$	$Pt_{21}Ir_{18}Co_{61}$	44	2.2 ± 0.2	3.3 ± 0.3	2.1	0.385

[a] Size-1(TEM): particle diameter (nm) of the as-synthesized nanoparticles determined by TEM. [b] Size-2(TEM): particle diameter (nm) of the nanoparticles supported on carbon after the thermal treatment determined by TEM. [c] Size-3(XRD): particle diameter (nm) of the nanoparticles supported on carbon after the thermal treatment estimated by XRD peak width.

the resulting trimetallic nanoparticles, which were determined by DCP-AES and ICP-OES, are compared with the synthetic feed ratios.

Overall, the relative compositions of Pt, Ir, and Co in the nanoparticles were found to scale with the feed ratio in the synthetic reaction solution in approximate linear relationships. Linear regressions for each metal component showed a slope of 0.95 for Pt, 0.94 for Ir, and 1.11 for Co, quite close to a 1:1 relationship between the feeding composition and the nanoparticle composition. The results thus demonstrate that the trimetallic compositions of the nanoparticles can be controlled by the metal-precursor concentrations and ratios.

Figure 2A shows a representative TEM image for a sample of as-synthesized $Pt_{25}Ir_{20}Co_{55}$ nanoparticles. Similar results have been obtained for PtIrCo nanoparticles with different compositions (Supporting Information, Figure S1). These nanoparticles display an average size of 2.5 nm, with a high monodispersity in size (±0.2 nm).

Carbon-Supported PtIrCo Catalysts. The carbon-supported PtIrCo nanoparticles (PtIrCo/C) with different trimetallic compositions after thermal treatment at 400 °C showed a metal loading of 44−52%. In general, the dispersion of the catalysts was quite good. The sizes of the nanoparticles for both $Pt_{65}Ir_{11}Co_{24}/C$ and $Pt_{40}Ir_{28}Co_{32}/C$ were found to increase slightly (by ∼1 nm) after the thermal treatment. The size monodispersity remained high (±0.3−0.4 nm). The $Pt_{25}Ir_{20}Co_{55}/C$ catalysts subjected to thermal treatment at higher temperatures were also examined. The size of the nanoparticles was found to increase from 3.3 nm in 400 °C to 7.0 nm in the case of 650 °C and to 10.1 nm in the case of 926 °C. The significant increase in particle size was attributed to a higher degree of sintering of nanoparticles because of close proximity of particles for these high metal-loading samples (40−50% metal loading on carbon). As shown in Table 1, there was no significant effect of the presence of different Co compositions in the examined Co-composition range on the particle size at higher temperatures. We also note that similar results have been observed for other nanoalloy catalysts that we studied previously, including PtCo/C[32] and PtNiCo/C catalysts.[31]

Nanoparticles and catalysts of other compositions and metal loadings were also examined. One example involved a study of $Pt_{61}Ir_{24}Co_{15}/C$ catalysts with a metal loading of 21−24% after thermal treatment at 400, 600, and 926 °C. The size of the nanoparticles was found to increase slightly from 2.0 to 2.3 nm for 400 °C, to 3.0 nm for 600 °C, and to 3.6 nm for 800 °C. In comparison with the previous high-loading catalysts, the observation of a much lower degree of sintering was attributed to lesser proximity of particles for these low metal-loading samples.

The understanding of the thermal processing parameters for the PtIrCo/C catalysts was an important part of our investigation for ensuring the removal of the capping materials and the calcination of the alloy. To find out the optimized thermal treatment condition, TGA experiments were carried out under various conditions. Under O_2 environment for the thermal treatment, severe burning of the PtIrCo/C catalysts at a relatively low temperature was found to be a major problem. As shown by the TGA data (Supporting Information, Figure S2), the removal of the organic shell begins at 180 °C in 20% O_2 +80% N_2 environments. However, burning of carbon was evident between 180 and 250 °C under 20% O_2 +80% N_2 environment. A more detailed study under N_2 in Figure 4a showed that the organic shell was removed effectively by thermal treatment under N_2 environment at about 280−300 °C. The TGA measurement of the catalysts (after thermal removal of capping molecules and the thermal calcination under H_2) showed that the carbon support was burned off completely between 300 and 350 °C, from which the metal loading was determined.

The detailed morphology and composition of the PtIrCo/C catalysts were further examined using HRTEM and EDS. As

dx.doi.org/10.1021/cs200022s |*ACS Catal.* 2011, 1, 562–572

shown in Figure 2B−C for $Pt_{25}Ir_{20}Co_{55}/C$ catalysts treated at 400 °C, the supported nanoparticles are small and crystalline. The lattice fringe, 0.223 nm, corresponds to the (111) plane of a face centered cubic (fcc) lattice which is found with bulk Pt and Ir. Note that bulk Co shows a hexagonal-type structure but when it is nanosized it may adopt an fcc-type structure.[39] For this sample, the composition ($Pt_{21}Ir_{18}Co_{61}/C$) after the thermal treatment was consistent with that of the original nanoparticles ($Pt_{25}Ir_{20}Co_{55}$), which was also supported by EDX data showing comparable Pt composition after the thermal treatment.

2. Alloying and Atomic-Scale Structure Properties. Catalysts with different composition, different loading, and treated at different temperatures were examined using the XRD technique. Figure 3 shows a representative set of XRD patterns for PtIrCo/C catalysts (44−55 wt %) with three different compositions thermally treated at 400 °C. The diffraction peaks are rather broad which is typical for nanosized materials. They appear at 2θ values that are rather close to the ones expected, i.e., 39.7 (111), 46.3 (200), and 67.3 (220) for fcc Pt, 41.0 (111), 47.5 (200), and 69.6 (220) for fcc Ir, and 44.3 (111), 51.6 (200), and 75.9 (220) for fcc Co. The 2θ peaks are shown to be closer to Pt and Ir fcc peaks rather than Co peaks, which can be explained by the alloying characteristic. Although the peaks are quite broad, there is no indication of a separate set of peaks for Co. Pt and Ir have very close 2θ values, but different from those of Co. The result indicates that the nanoparticles have an fcc-type structure without signatures of phase segregation. The particle sizes calculated from the peak widths using the Scherrer equation and the respective fcc lattice parameters calculated from the peak positions are given in Table 1. The particle sizes are comparable with those determined from the TEM data. As expected, the lattice parameters are found to be dependent on the trimetallic composition.

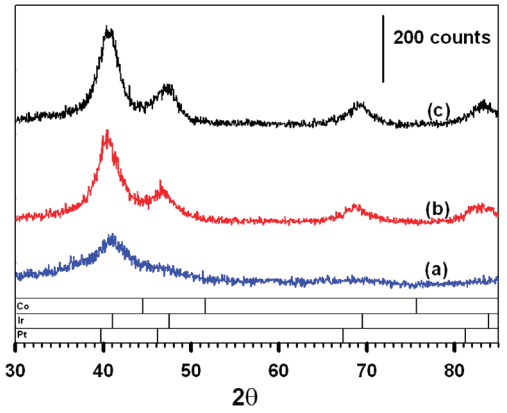

Figure 3. XRD patterns of the catalysts: (a) $Pt_{25}Ir_{20}Co_{55}/C$, (b) $Pt_{40}Ir_{28}Co_{32}/C$, and (c) $Pt_{65}Ir_{11}Co_{24}/C$ treated at 400 °C (44−52 wt %). Bottom: Standard 2θ peaks of Pt, Ir, and Co.

Figure 4A shows the HE-XRD pattern for $Pt_{25}Ir_{20}Co_{55}/C$ treated at 400 °C. Thanks to the usage of higher-energy X-rays many more diffraction features were detected as compared to the Cu Kα XRD data in Figure 3. Atomic PDF extracted from the HE-XRD data is shown in Figure 4B together with the PDF of a 2.5 nm, pure Pt standard. The PDFs show a sequence of peaks, that is, atomic coordination spheres that are characteritic for an fcc-type structure confirming that the trimetallic nanoparticles studied here are an fcc-type alloy. The coordination spheres in the $Pt_{25}Ir_{20}Co_{55}/C$ appear at interatomic distances that are slightly shorter than those in pure Pt since the size of Co (∼1.35 Å) and Ir (∼1.36 Å) atoms is smaller than that of Pt (∼1.39 Å) atoms. Also, the PDF shows well-defined peaks up to about 20 Å, that is, up to distances comparable to the nanoparticle size, indicating that the fcc-type structure of the nanoparticles is well-defined despite their small size. A further modeling analysis of the PDF data is in progress for determining precisely the alloy ordering/disordering parameters of the trimetallic nanoparticles.

Figure 5A shows another representative set of XRD patterns for $Pt_{25}Ir_{20}Co_{55}/C$ catalysts with a higher loading (44−50 wt %) and treated at different temperatures. The metal loading was found to increase from 44% for the catalyst treated at 400 °C to 50% for treatment at 650 and 926 °C, likely because of a slight gasification of carbon support at higher temperatures. As shown in Table 2, a considerable shrinking of the fcc-type lattice parameter, a, is observed as the thermal treatment temperature is increased from 400 °C (a = 0.385 nm) to 650 °C, (a = 0.379 nm) and then to 926 °C (a = 0.374 nm). In this case, the particle size was found to increase dramatically from 3.3 to 10 nm because of sintering of nanoparticles for these high metal-loading samples (40−50% metal loading on carbon), in agreement with the TEM measurement results.

Catalysts with a lower loading treated at different temperatures were also examined. Figure 5B shows a representative set of XRD patterns for $Pt_{61}Ir_{24}Co_{15}/C$ catalysts with 21−24 wt % loading treated at different temperatures. The initial metal loading at

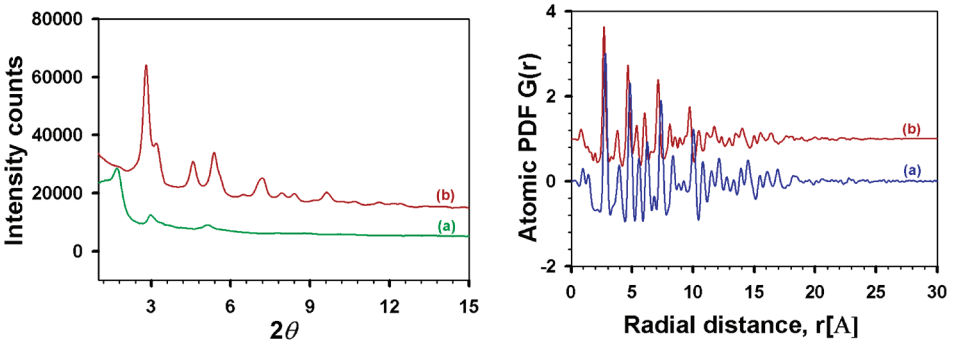

(A) (B)

Figure 4. HE-XRD patterns for $Pt_{25}Ir_{20}Co_{55}/C$ treated at 400 °C: (A) The intensity plots comparing $Pt_{25}Ir_{20}Co_{55}/C$ (b) with pure carbon (a); (B) atomic PDFs versus radial distance, r (in Å), for $Pt_{25}Ir_{20}Co_{55}/C$ (b) and pure Pt standard (a).

dx.doi.org/10.1021/cs200022s |ACS Catal. 2011, 1, 562–572

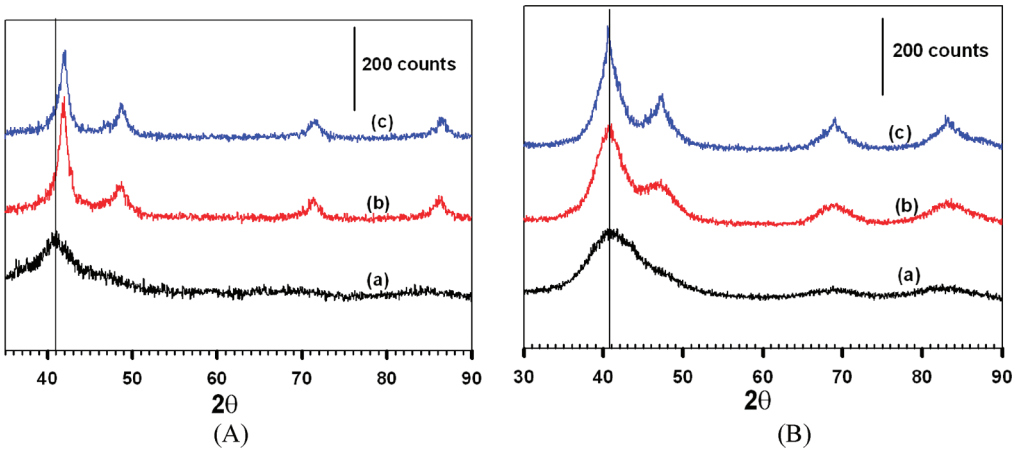

Figure 5. XRD patterns: (A) $Pt_{25}Ir_{20}Co_{55}$/C catalysts treated at 400 °C (a), 650 °C (b), and 926 °C (c) (44−50 wt %). (B) $Pt_{61}Ir_{24}Co_{15}$/C catalysts (21−24 wt %) treated at 400 °C (a), 600 °C (b), and 800 °C (c).

Table 2. Summary of the fcc-Type Lattice Parameters for $Pt_{25}Ir_{20}Co_{55}$/C and $Pt_{61}Ir_{24}Co_{15}$/C Catalysts Treated at Different Temperatures (T)

composition NPs	T °C	M (wt %)	size-1(TEM) (nm)[a]	size-2(TEM) (nm)[b]	size-3(XRD) (nm)[c]	lattice parameter (nm)
$Pt_{25}Ir_{20}Co_{55}$	400	44	2.2 ± 0.2	3.3 ± 0.3	2.1	0.385
$Pt_{25}Ir_{20}Co_{55}$	650	50	2.2 ± 0.2	7.0 ± 1.4	6.8	0.379
$Pt_{25}Ir_{20}Co_{55}$	926	50	2.2 ± 0.2	10.1 ± 2.4	7.7	0.374
$Pt_{61}Ir_{24}Co_{15}$	400	21	2.0 ± 0.2	2.3 ± 0.4	2.1	0.387
$Pt_{61}Ir_{24}Co_{15}$	600	23	2.0 ± 0.2	3.0 ± 0.2	2.4	0.386
$Pt_{61}Ir_{24}Co_{15}$	800	24	2.0 ± 0.2	3.6 ± 0.3	4.8	0.385

[a] Size-1(TEM): particle diameter (nm) of the as-synthesized nanoparticles determined by TEM. [b] Size-2(TEM): particle diameter (nm) of the nanoparticles supported on carbon after the thermal treatment determined by TEM. [c] Size-3(XRD): particle diameter (nm) of the nanoparticles supported on carbon after the thermal treatment estimated by XRD peak width.

Table 3. Structural Parameters from Fitting of EXAFS Data at Pt L3 Edge for $Pt_{40}Ir_{28}Co_{32}$/C Treated at 400 °C

scatterer	N	R bond length (Å)	disorder ($\times 10^{-3}$ Å^2)
Pt−Co	0.5 ± 0.6	2.66 ± 0.04	1.9 ± 6.7
Pt−Pt	6.3 ± 1.9	2.73 ± 0.01	6.1 ± 1.3

400 °C was 21%, which increased to 24% when the catalyst was treated at 600 and 800 °C. As shown in Table 2, the size increase is comparatively less dramatic in comparison with those with higher metal loading. The (111) and (200) peaks are not resolved for the 400 °C treated sample. As the temperature increased, the (111) and (200) plane peaks become clearly separated as a result of the particle size increase. The fcc-type lattice parameter was found to decrease as the thermal treatment temperature increased. The rate of decrease is, however, somewhat smaller in comparison with that for the catalysts with 50% metal loading (Table 2). This difference is likely due to the different Co content in these two catalysts. According to Vegard's Law, the lattice constant of an alloy can be estimated based on the alloy composition and the lattice constants of the end members of the alloy. For $Pt_{25}Ir_{20}Co_{55}$, the lattice constant is expected to be ~0.369 nm assuming a 100% alloying of Pt and Ir that is known to have very similar fcc-lattice constants. Apparently, the thermal treatment at 400 °C did not form a perfectly uniform (i.e., random) alloy. A large amount of Co atoms may not be quite randomly alloyed with Pt and Ir, forming localized Co or Co oxide clusters. The higher annealing temperatures led to the formation of a more uniform alloy than those at lower temperatures. Similar phenomena have been observed for PtNiCo/C alloy catalysts synthesized by the nanoengineered synthesis and processing method.[31] For $Pt_{61}Ir_{24}Co_{15}$ /C, which has a much lower Co content, a lattice constant around 0.385 is expected assuming a 100% alloying. On the basis of the XRD data in Table 3, it appears that it is much easier to form a uniform alloy for nanoparticles with a low Co content at low temperature.

To gain further insights into the coordination structures of these catalysts, XAFS measurements were carried out with $Pt_{40}Ir_{28}Co_{32}$/C (4.4 ± 0.3 nm). Figure 6a shows normalized Pt L3 edge XANES spectra of the catalyst and a Pt foil. The white line (at ~11,567 eV) intensity of the catalyst is higher than that of the Pt foil, indicative of the decrease of 5d orbital filling in the Pt alloys because of oxidation and hybridization (i.e., an increase in Pt d-band vacancy). In addition, oscillations due to a Ir L3 edge are observed at the pre-edge region between 11200 and 11400 eV. The Ir oscillations leak into a Pt L3 edge EXAFS and affect mostly its low-k region. As a result, the coordination of oxygen around Pt cannot be determined by fitting of the Pt EXAFS data. Figure 6b presents normalized Co K edge XANES spectra of the catalyst and a Co foil. Compared with the XANES spectra of Co oxides in the literature,[40] the detected Co in the catalyst is mostly in the oxide form in view of the similarity of the spectrum to that of Co_3O_4.

More quantitative structural information is obtained through fitting of the EXAFS data. The results from fits of the magnitude

dx.doi.org/10.1021/cs200022s |ACS Catal. 2011, 1, 562–572

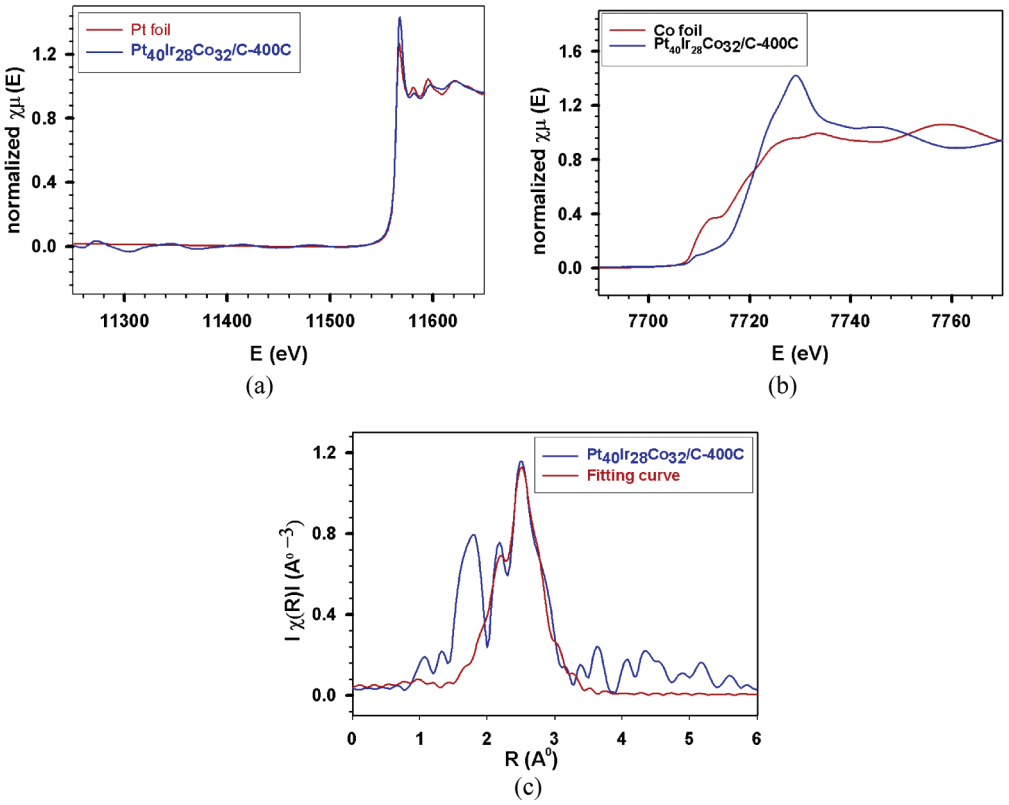

Figure 6. Normalized XANES spectra at Pt L_3 edge (a) and Co K edge (b) for $Pt_{40}Ir_{28}Co_{32}/C$ treated at 400 °C. Pt foil and Co foil are used as standards. Data and fit (c) of the magnitude of Fourier transformed k^2-weighted Pt L3 edge EXAFS spectra (R-bond length in Å).

of Fourier transformed k^2-weighted Pt L3 edge EXAFS spectra are shown in Figure 6c. Good fit is obtained for the range between 2.0 and 3.2 Å in *R* space, representing Pt (or Ir) and/or Co around Pt in the first coordination shell. There is some Pt in oxide form, and oxygen would appear in an *R* less than 2 Å because of phase shift (Pt−O bond distance is close to 2 Å). The intense peak around 1.7 Å of the catalyst in Figure 6c cannot be fitted using the Pt−O path because of the interference from Ir L3 edge EXAFS as discussed earlier. The structural parameters obtained from the fitting are listed in Table 3. Except oxygen, it is clearly shown that the majority of the nearest neighbors around Pt are Pt. Note that Ir and Pt have almost identical photoelectron scattering properties which cause the EXAFS oscillations since they have almost identical atomic number (or number of electrons) and atomic radius. In fact, replacing Pt with Ir does not change the fitting results. Though addition of Pt−Co path in the fitting improves the fit, the uncertainties associated with Pt−Co path are very big, which indicates rather the presence of Co in the first coordination shell around Pt. This observation is consistent with the Co K-edge XANES results that there is a significant amount of Co which exists in oxide form. In short, the XAFS results strongly suggest that most Pt forms Pt−Ir alloy with enriched Pt along with some oxides, which is consistent with a slight reduction of the interatomic distance in the fcc-type lattice parameter for the alloy catalyst in comparison with pure Pt, as revealed by HE-XRD data.

The trimetallic catalysts were also examined using X-ray photoelectron spectroscopy (XPS) to gain an understanding of the relative surface properties of the electrocatalysts (Supporting Information, Figure S3). For example, for $Pt_{25}Ir_{20}Co_{55}/C$ treated at 400 °C, Pt $4f_{7/2}$ and Pt $4f_{5/2}$ bands were observed at 72.1 and 75.4 eV, Ir $4f_{7/2}$ and Ir $4f_{5/2}$ peaks were observed at 61.4 and 64.3 eV, and Co $2p_{3/2}$ and Co $2p_{1/2}$ peaks were observed at 780.0 and 796.0 eV, respectively. The binding energies for Pt and Ir are basically consistent with those reported previously for other alloy catalysts.[31,41] For Co, the basic characteristic for the Co 2p peak is similar to those for other ternary catalysts (e.g., PtNiCo[31]) in terms of binding energy. The peaks from spectral deconvolution of the $Co2p_{3/2}$ spectral region (Supporting Information, Figure S3) were found at 779.4 eV for Co^0, 781.6 eV for Co(2+), and 786.2 eV for Co(3+) species, demonstrating the presence of Co in both metallic form and oxide form. On the basis of the combined results from XRD, XAFS, and XPS characterizations, we believed that both Co and Co oxide are present in the trimetallic nanoparticles, though their relative percentages are yet to be determined.

3. Electrocatalytic Activity and Durability. Electrochemical active area (ECA), mass activity (MA), and specific activity (SA) for the PtIrCo catalysts were determined from measurements of CV and RDE curves. The electrochemical measurements were performed after potential cycling of the catalysts for 50 cycles between 0.02 and 1.2 V to remove Co and Co oxides on the surface. Figure 7A shows a typical set of cyclic voltammetric curves for the PtIrCo/C catalysts with different compositions ($Pt_{65}Ir_{11}Co_{24}/C$, $Pt_{40}Ir_{28}Co_{32}/C$, and $Pt_{25}Ir_{20}Co_{55}/C$ thermally treated at 400 °C). As evidenced by the CV curves, the characteristics in the hydrogen adsorption/desorption region showed subtle differences. The hydrogen adsorption/desorption peaks are not clearly resolved, which is typical for Pt alloy nanocatalysts. The Pt−OH reduction peak at 0.6−0.8 V showed

dx.doi.org/10.1021/cs200022s |*ACS Catal.* 2011, 1, 562–572

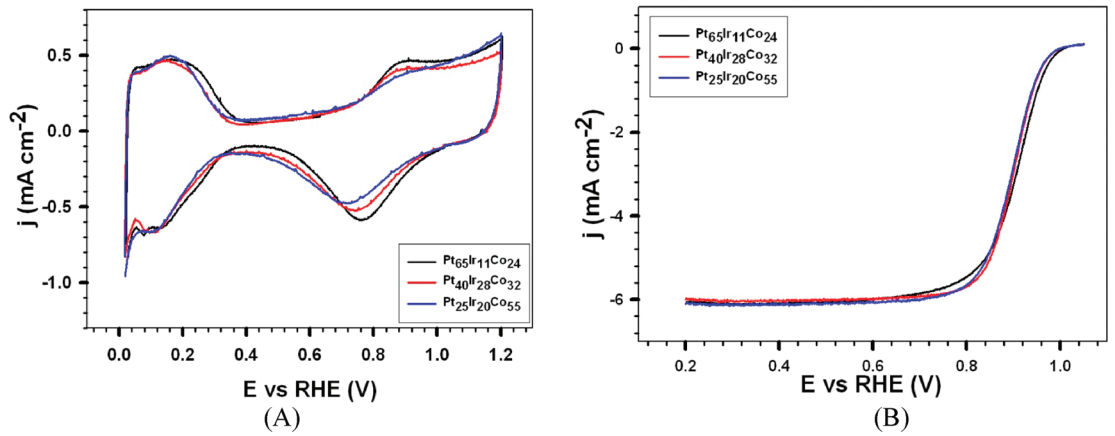

Figure 7. (A) CV curves in 0.1 M $HClO_4$, which were recorded after 50 potential cycles in the range of 0.02 V−1.2 V with a scan rate of 100 mV/s in N_2-saturated solution. (B) RDE curves in O_2-saturated 0.1 M $HClO_4$, which were recorded after 50 potential cycles in the range of 0.02 V−1.2 V. Scanning rate: 10 mV/s. The catalysts: (a) $Pt_{65}Ir_{11}Co_{24}$/C, (b) $Pt_{40}Ir_{28}Co_{32}$/C, and (c) $Pt_{25}Ir_{20}Co_{55}$/C treated at 400 °C. Pt loading = 16, 10, and 7 $\mu g/cm^2$ on the electrode for samples a, b, and c, respectively.

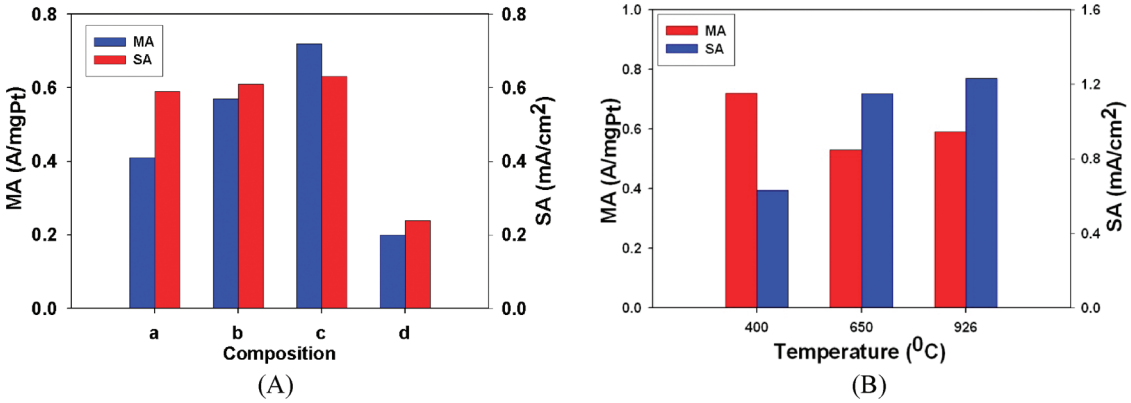

Figure 8. Comparison of mass activity (MA) and specific activity (SA) data for catalysts with different compositions. (A) (a) $Pt_{65}Ir_{11}C0_{24}$/C, (b) $Pt_{40}Ir_{20}Co_{32}$/C, (c) $Pt_{25}Ir_{20}Co_{55}$/C, and (d) Pt/C (TKK, 50% wt.); (B) $Pt_{25}Ir_{20}Co_{55}$/C catalysts treated at different temperatures.

a considerable shift to a higher potential as the amount of Pt increases in the composition. The difference of ~20 mV at half wave potential between the alloy catalysts may be attributed to the difference of oxidation/reduction potentials on PtIrCo catalysts with different compositions. The ECA values were found to be ranging from 70 to 120 m^2/g_{Pt}. Note that Ir also has similar voltammetric features in the hydrogen adsorption/desorption region to Pt, resulting in an overestimated ECA value for PtIrCo alloys.

Nevertheless, the ECA values are clearly higher than those reported for $Pt_{75}Ir_{12.5}X_{12.5}$ (X = Co, Ni, V) catalysts (2−5 nm) prepared by a carbothermal synthesis route (50−60 m^2/g).[29,30] This difference could reflect a combination of the smaller size with high monodispersity and the better dispersion for the carbon-supported PtIrCo nanoparticles prepared by the nanoengineered synthesis and processing route.

The ORR activities of PtIrCo were measured by RDE, and the polarization curves were shown in Figure 8B. Considering the fact that there were differences in Pt loading (i.e., 16, 10, and 7 $\mu g/cm^2$ on the electrode for $Pt_{65}Ir_{11}Co_{24}$/C(a), $Pt_{40}Ir_{28}Co_{32}$/C(b), and $Pt_{25}Ir_{20}Co_{55}$/C(c)), the changes of the kinetic currents with the composition of the nanoparticles are translated to changes in mass activity and specific activity of the catalysts as shown in Figure 8, where the mass activity and specific activity data obtained from the kinetic current at 0.9 V are plotted as function of the nanoparticle composition treated at 400 °C. The Pt mass activities are 0.41, 0.57, and 0.72 A/mg_{Pt} for $Pt_{65}Ir_{11}C0_{24}$/C, $Pt_{40}Ir_{20}Co_{32}$/C, and $Pt_{25}Ir_{20}Co_{55}$/C, respectively. In comparison with the mass activity for Pt/C catalysts (0.2 A/mg_{Pt}), the mass activity was increased by a factor of 2−4 for these catalysts.

There is a clear trend showing the increase of the mass activity with the increase of Co% and the decrease of Pt% in the nanoparticles. In comparison with the specific activity for Pt/C catalysts (0.24 mA/cm^2), the specific activity was increased by a factor of ~3 for these catalysts. The fact that the specific activity (~0.6 mA/cm^2) did not show any significant change with the trimetallic composition could be accounted for by considering a combination of other structural factors, including the degree of alloying, the lattice strain, and the particle size. As shown in Table 1, $Pt_{65}Ir_{11}Co_{24}$/C and $Pt_{40}Ir_{28}Co_{32}$/C have a very similar fcc-type lattice constant (0.387 nm for $Pt_{65}Ir_{11}Co_{24}$/C, and 0.389 nm for $Pt_{40}Ir_{28}Co_{32}$/C). The fcc-type lattice shrinking is apparently insignificant for these catalysts treated at 400 °C. In addition, they also have a similar particle size (~4 nm). Therefore, it is reasonable for $Pt_{65}Ir_{11}Co_{24}$/C and $Pt_{40}Ir_{28}Co_{32}$/C to

dx.doi.org/10.1021/cs200022s |ACS Catal. 2011, 1, 562–572

Table 4. Summary of the Physical and Electrochemical Parameters for PtIrCo/C Catalysts with Different Compositions and Thermal Treatment Temperatures

composition NPs	temp °C	metal loading (%*wt*)	lattice parameter (nm)	ECA (m^2/g_{Pt})	MA (A/mg_{Pt})	MA (A/mg_{PGM})	SA (mA/cm^2)
$Pt_{65}Ir_{11}Co_{24}$	400	52	0.387	70	0.41	0.35	0.59
$Pt_{40}Ir_{28}Co_{32}$	400	44	0.389	93	0.57	0.34	0.61
$Pt_{25}Ir_{20}Co_{55}$	400	44	0.385	116	0.72	0.40	0.63
$Pt_{25}Ir_{20}Co_{55}$	650	50	0.379	46	0.53	0.29	1.15
$Pt_{25}Ir_{20}Co_{55}$	926	50	0.374	46	0.59	0.33	1.23

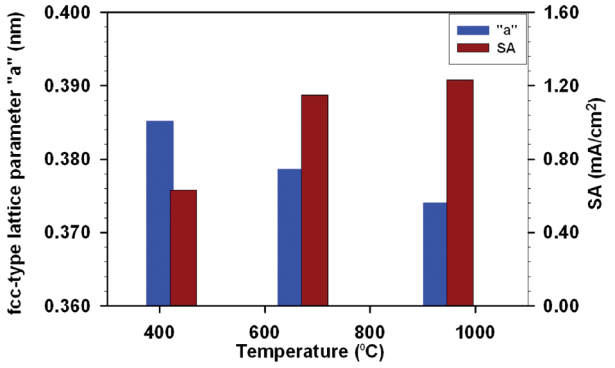

Figure 9. Comparison of the ORR specific activity and the fcc-type lattice parameter "*a*" as a function of thermal treatment temperatures for $Pt_{25}Ir_{20}C0_{55}/C$ catalysts.

exhibit a similar specific activity. The fcc-type lattice constant for $Pt_{25}Ir_{20}Co_{55}/C$ (0.385 nm) is smaller than that of $Pt_{65}Ir_{11}Co_{24}/C$ and $Pt_{40}Ir_{28}Co_{32}/C$ because of a larger Co content in the alloy. The specific activity of $Pt_{25}Ir_{20}Co_{55}/C$ is expected to be enhanced because of a combination of the fcc-type lattice shrinking and the decrease of 5d orbital filling in the Pt alloys as revealed by the XAFS data.[39] The increased amount of Co in $Pt_{25}Ir_{20}Co_{55}/C$ in comparison with $Pt_{65}Ir_{11}Co_{24}/C$ and $Pt_{40}Ir_{28}Co_{32}/C$ and its tendency of oxidation could also lead to the increase of d-band vacancy, which is known to have a significant effect on the electrocatalytic activity.[42−46] However, the specific activity of the trimetallic alloy catalysts also depends on the particle size. The ORR activity of PtCo/C is recently shown to be size dependent, exhibiting an initial increase with the particle size with a maximum mass activity around 4.5 nm.[21] In our recent study of PtCo/C catalysts prepared by a method similar to the PtIrCo/C catalysts, a decrease in mass activity and specific activity was observed with increasing particle size.[32] Because the particle size of $Pt_{25}Ir_{20}Co_{55}/C$ (3 nm) is smaller than those of $Pt_{65}Ir_{11}Co_{24}/C$ and $Pt_{40}Ir_{28}Co_{32}/C$, the enhancement of the specific activity from the catalyst with a small fcc-type lattice constant may be offset by a small particle size. We also note that the increase in specific activity over Pt/C catalysts (a factor of ∼3) is higher than those reported for PtIrCo/C (a factor of ∼2) prepared by a carbothermal synthesis route.[28−30] The surface alloying also has a significant effect on the adsorption of OH on the catalyst. When Pt and Ir atoms are mixed on the surface of the catalyst, the OH adsorbed on Ir at low potentials has a repulsion effect on the OH and oxide formation on Pt, resulting in higher ORR kinetics because of a lower OH coverage on Pt.[47]

To examine the effect of the thermal treatment temperature on the activities, the activities of $Pt_{25}Ir_{20}Co_{55}/C$ catalysts annealed at 400, 650, and 926 °C were compared (Figure 8). It is evident that the mass activity of the catalyst decreases with the increase in temperature. There was a dramatic decrease in the ECA with the increase in temperature. This can be attributed to substantial sintering of the nanoparticles at higher temperatures which is favorable because of the high metal loading on carbon (∼50 wt %), as shown in Table 2. Table 4 summarizes the data. It is interesting to note that the specific activity increases to almost double of that for the catalysts treated at the lower temperatures (Figure 8B). In comparison with the specific activity for Pt/C catalysts (0.24 mA/cm^2), the specific activity was increased by a factor of ∼5 for 650−926 °C treated catalysts. In this case, the MA was found to decrease slightly. Since the particle size was found to increase while the lattice parameter decreased with the thermal treatment temperature, the doubling of the SA values from 0.63 at 400 °C to 1.13 at 650 °C is believed to reflect a combination of particle size and atomic-scale structure effects on the electrocatalytic activity.

As shown in Figure 9, the specific activity showed an increase as a result of the increased treatment temperature from 400 to 926 °C. In contrast, the lattice parameter displayed a clear decrease with the increase in thermal treatment temperature. It is thus evident that the increase in the specific activity is correlated with the decrease in the lattice parameter for these catalysts.

For this set of catalysts, there was a relatively large increase in particle size with the increase in thermal treatment temperature (from 3.3 to 10 nm). A further study is in progress to understand the detailed atomic-scale structure-activity correlation for catalysts with a lower metal loading, minimizing the sintering of nanoparticles, and controlling the size changes. It is evident that the combination of the particle size increase and atomic-scale structure changes, in particular lattice shrinking, played a significant role in increasing the specific activity.

The durability of the PtIrCo catalysts was also examined in the O_2-saturated 0.1 M $HClO_4$ based on a square-wave potential cycling protocol (see Experimental Section, and Supporting Information, Figure S4). The catalysts were cycled, keeping the potential at 0.65 and 1.2 V for 5 s each. The ECA and ORR activity data were measured in a fresh 0.1 M $HClO_4$ solution after every 5000 cycles. A representative set of the results is shown in Figure 10 for $Pt_{65}Ir_{11}Co_{24}/C$ (52%) catalyst treated at 400 °C in comparison with those for commercially available catalysts Pt/C (TKK, 46%) and Pt_3Co/C (TKK, 46%). Note that the average particle sizes derived from TEM for Pt/C, Pt_3Co/C, and $Pt_{65}Ir_{11}Co_{24}/C$ are 2.8, 4.1, and 3.6 nm, respectively. The initial mass activities for Pt/C, Pt_3Co/C, and $Pt_{65}Ir_{11}Co_{24}/C$, are 0.2, 0.46, and 0.41 A/mg, respectively. The changes of the particle size and lattice constants after the potential cycling have not been measured yet for this particular system since the work reported here focuses on the as-prepared catalysts. The study of the catalyst durability is part of our ongoing work, as we have

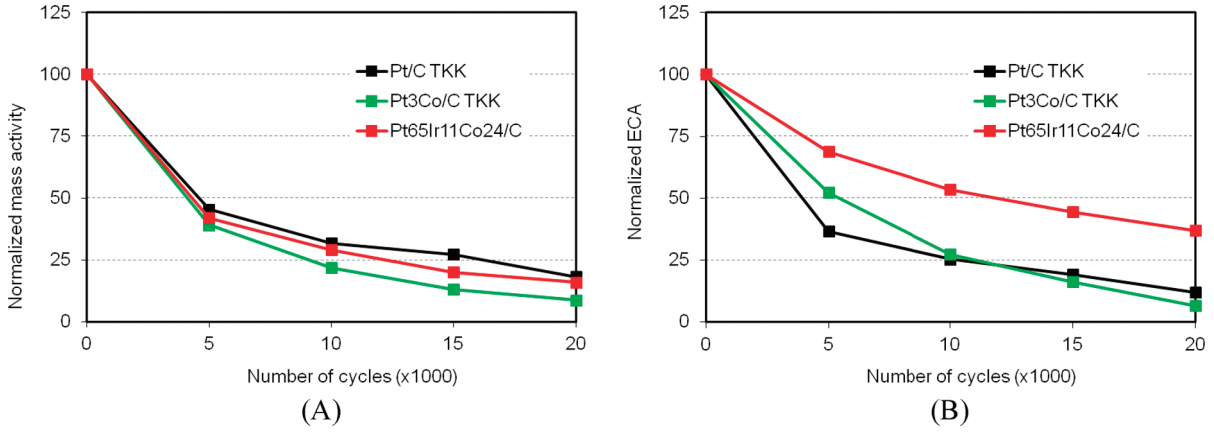

Figure 10. Plots of normalized mass activities (A) and ECA values (B) as a function of the number of potential cycles(ranging from 0 to 20,000 cycles) for different catalysts upon potential cycling.

recently done for other catalyst systems such as PtVFe/C catalysts.[48]

As expected, most of the mass activity loss for all the samples occurred during the initial 5000 cycles (Figure 10A). In comparison with those for the commercial catalysts, the rate of the mass activity loss of $Pt_{65}Ir_{11}Co_{24}/C$ was comparable to that of Pt/C and slightly lower than that of Pt_3Co/C. After 20000 cycles, the mass activity of $Pt_{65}Ir_{11}Co_{24}/C$ (0.06 A/mg) was higher than that of Pt/C and Pt_3Co/C (0.04 A/mg). The rate of ECA loss of $Pt_{65}Ir_{11}Co_{24}/C$ during potential cycling was two times lower than those of commercial catalysts (Figure 10B). After 20000 cycles, the ECA of $Pt_{65}Ir_{11}Co_{24}/C$ changes from 70 to 25 m^2/g, while the ECA decreases from 82 to 10 m^2/g for Pt/C, and from 49 to 3 m^2/g for Pt_3Co/C. These findings demonstrated that the $Pt_{65}Ir_{11}Co_{24}/C$ catalyst synthesized by our synthesis and processing method has a comparable durability to that of commercial catalysts upon the severe potential cycling. It is important to note that RDE and CV are currently considered as standard methods for assessing the mass activity and specific activity of Pt-alloy catalysts, as shown in most of the literature reports. The comparability of fuel-cell tests and RDE/CV based measurements has been discussed by Gasteiger et al.[49] For practical applications, there is no question that fuel cell durability testing is important, which is in fact part of our ongoing work, as we have recently demonstrated for other Pt-alloy catalysts such as PtVFe/C and AuPt/C.[17,18,48,50]

CONCLUSIONS

In conclusion, the relative compositions of Pt, Ir, and Co in the trimetallic PtIrCo nanoparticles with controlled size (1−3 nm) prepared by the nanoengineered synthesis and processing method have been shown to be controllable by the feed ratio of the metal precursors in the synthetic reaction solution. The nanoparticles supported on carbon black and thermally treated under different environments showed a subtle but controllable increase in particle size, depending on the temperature of treatment and the metal loading. The nanoparticle catalysts were found to display a fcc-type structure. No apparent phase segregation was observed even at high temperatures. An increase in the mass activity was observed with the decrease of Pt% and the increase of Co% in the composition of the nanoparticles. The electrocatalytic specific activity for oxygen reduction reaction showed an increase by a factor of 3−5 for the PtIrCo/C catalysts in comparison with Pt/C catalysts. The specific activity has been shown to correlate with the structural parameters such as size, composition, and fcc-type lattice parameter. The specific activity increases whereas the lattice parameter decreases with the thermal treatment temperature. The presence of Ir in the trimetallic alloy could also play an important role in the increase of the stability of the catalysts. A detailed study of the correlation between the atomic-scale structure and the electrocatalytic activity and the performance of the catalysts in PEMFCs is part of our ongoing work.

ASSOCIATED CONTENT

Supporting Information. Additional TEM micrographs and size distributions for as-synthesized PtIrCo nanoparticles of different compositions (Figure S1), TGA curves for thermal treatment (Figure S2), XPS data for catalyst composition (Figure S3), and electrochemical data for catalyst durability study (Figure S4). This material is available free of charge via the Internet at http://pubs.acs.org.

AUTHOR INFORMATION

Corresponding Author

*E-mail: cjzhong@binghamton.edu (C.J.Z.), minhua.shao@utcpower.com (M.S.).

ACKNOWLEDGMENT

This work was supported by UTC Power and in part by the NSF(CBET-0709113). We also thank Dr. H. R. Naslund (Department of Geological Sciences, SUNY-Binghamton) for assistance in DCP-AES analysis, Dr In-Tae Bae (S3IP, SUNY-Binghamton) for the HRTEM analysis, and Mr. Mark H. Engelhard for XPS analysis at EMSL, a national scientific user facility sponsored by DOE's Office of Biological and Environmental Research located at PNNL. MRCAT operations are supported by the Department of Energy and the MRCAT member institutions.

REFERENCES

(1) Seo, A.; Lee, J.; Han, K.; Kim, H. *Electrochim. Acta* **2006**, *52*, 1603–1611.

(2) Bogdanovskaya, V. A.; Tarasevich, M. R.; Kuznetsova, L. N.; Radina, M. V. *Russ. J. Phys. Chem. A* **2009**, *83*, 2045–2049.

(3) Shukla, A. K.; Neergat, M.; Bera, P.; Jayaram, V.; Hegde, M. S. *J. Electroanal. Chem.* **2001**, *504*, 111–119.
(4) Aricò, A. S.; Shukla, A. K.; Kim, H.; Park, S.; Min, M.; Antonucci, V. *Appl. Surf. Sci.* **2001**, *172*, 33–40.
(5) Freund, A.; Lang, J.; Lehmann, T.; Starz, K. A. *Catal. Today* **1996**, *27*, 279–283.
(6) Jeon, M. K.; Cooper, J. S.; McGinn, P. J. *J. Power Sources* **2009**, *192*, 391–395.
(7) Jeon, M. K.; McGinn, P. J. *J. Power Sources* **2009**, *194*, 737–745.
(8) Toda, T.; Igarashi, H.; Uchida, H.; Watanabe, M. *J. Electrochem. Soc.* **1999**, *146*, 3750–3756.
(9) Lukaszewski, M.; Kedra, T.; Czerwinski, A. *J. Electroanal. Chem.* **2010**, *638*, 123–130.
(10) Hwang, J. T.; Chung, J. S. *Electrochim. Acta* **1993**, *38*, 2715–2723.
(11) Luo, J.; Han, L.; Kariuki, N. N.; Wang, L.; Mott, D.; Zhong, C. J.; He, T. *Chem. Mater.* **2005**, *17*, 5282.
(12) Luo, J.; Wang, L.; Mott, D.; Njoki, P. N.; Kariuki, N. N.; Zhong, C. J.; He, T. *J. Mater. Chem.* **2006**, *16*, 1665.
(13) Luo, J.; Kariuki, N.; Han, L.; Wang, L.; Zhong, C. J.; He, T. *Electrochim. Acta* **2006**, *51*, 4281–4827.
(14) Zhong, C. J.; Luo, J.; Njoki, P. N.; Mott, D.; Wanjala, B.; Loukrakpam, R.; Lim, S.; Wang, L.; Fang, B.; Xu, Z. *Energy Environ. Sci.* **2008**, *1*, 454–466.
(15) Zhong, C. J.; Luo, J.; Fang, B.; Wanjala, B. N.; Njoki, P. N.; Loukrakpam, R.; Yin, J. *Nanotechnology* **2010**, *21*, 062001.
(16) Sun, S.; Murray, C. B.; Weller, D.; Folks, L.; Moser, A. *Science* **2000**, *287* (5460), 1989–1992.
(17) Fang, B.; Luo, J.; Njoki, P. N.; Loukrakpam, R.; Mott, D.; Wanjala, B.; Hu, X. *Electrochem. Commun.* **2009**, *11*, 1139–1141.
(18) Fang, B.; Luo, J.; Njoki, P. N.; Loukrakpam, R.; Wanjala, B.; Hong, J.; Yin, J.; Hu, X.; Last, J.; Zhong, C. J. *Electrochim. Acta* **2010**, *55*, 8230–8236.
(19) Stamenkovic, V.; Mun, B. S.; Mayrhofer, K. J. J.; Ross, P. N.; Markovic, N. M.; Rossmeisl, J.; Greeley, J.; Nørskov, J. K. *Angew. Chem., Int. Ed.* **2006**, *45*, 2897–2901.
(20) Stamenkovic, V. R.; Mun, B. S.; Arenz, M.; Mayrhofer, K. J. J.; Lucas, C. A.; Wang, G. F.; Ross, P. N.; Markovic, N. M. *Nat. Mater.* **2007**, *6*, 241–247.
(21) Wang, C.; van der Vliet, D.; Chang, K.-C.; You, H.; Strmcnik, D.; Schlueter, J. A.; Markovic, N. M.; Stamenkovic, V. R. *J. Phys. Chem. C* **2009**, *113*, 19365–19368.
(22) Qiao, J.; Li, B.; Ma, J. *J. Electrochem. Soc.* **2009**, *156*, B436–B440.
(23) Shan, C.-C.; Tsai, D.-S.; Huang, Y.-S.; Jian, S.-H.; Cheng, C.-L. *Chem. Mater.* **2007**, *19*, 424–431.
(24) Jung, H.-Y.; Park, S.; Popov, B. N. *J. Power Sources* **2009**, *191*, 357–361.
(25) Yim, S.-D.; Park, G.-G.; Sohn, Y.-J.; Lee, W.-Y.; Yoon, Y.-G.; Yang, T.-H.; Um, S.; Yu, S.-P.; Kim, C.-S. *Int. J. Hydrogen Energy* **2005**, *30*, 1345–1350.
(26) Yim, S.-D.; Lee, W.-Y.; Yoon, Y.-G.; Sohn, Y.-J.; Park, G.-G.; Yang, T.-H.; Kim, C.-S. *Electrochim. Acta* **2004**, *50*, 713–718.
(27) Holt-Hindle, P.; Yi, Q.; Wu, G.; Koczkur, K.; Chen, A. *J. Electrochem Soc.* **2008**, *155*, K5–K9.
(28) Protsailo, L. In *DOE Hydrogen and Fuel Cell Review Meeting*, 2006; U.S. Department of Energy.
(29) Motupally, S. In *DOE Hydrogen and Fuel Cell Review Meeting*, 2008; U.S. Department of Energy.
(30) Srinivasamurthi, V. In *DOE Hydrogen and Fuel Cell Review Meeting*, 2009; U.S. Department of Energy.
(31) Wanjala, B. N.; Loukrakpam, R.; Luo, J.; Njoki, P. N.; Mott, D.; Zhong, C. J.; Shao, M.; Protsailo, L.; Kawamura, T. *J. Phys. Chem. C.* **2010**, *114*, 17580–17590.
(32) Loukrakpam, R.; Luo, J.; He, T.; Chen, Y.; Xu, Z.; Njoki, P. N.; Wanjala, B. N.; Fang, B.; Mott, D.; Yin, J.; Klar, J.; Powell, B.; Zhong, C. J. *J. Phys. Chem. C* **2011**, *115*, 1682–1694.
(33) Ma, Y.; Balbuena, P. B. *J. Electrochem. Soc.* **2010**, *157* (6), B959–B963.
(34) Egami, T.; Billinge, S. J. L., Ed., *Underneath the Braggs' Peak*; Pergamon Press: Amsterdam, The Netherlands, 2003.
(35) Petkov, V. *Mater. Today* **2008**, *11*, 28–38.
(36) Ravel, B.; Newville, M. *J. Synchrotron Radiat.* **2005**, *12*, 537–541.
(37) Newville, M. *J. Synchrotron Radiat.* **2001**, *8*, 322–324.
(38) Rehr, J. J.; Albers, R. C. *Rev. Modern Phys.* **2000**, *72*, 621–654.
(39) Owen, E. A.; Jones, D. M. *Proc. Phys. Soc.* **1954**, *B 67*, 456–466.
(40) Chadwick, A. V.; Savin, S. L. P.; Alcántara, R.; Lisbona, D. F.; Lavela, P.; Ortiz, G. F.; Tirado, J. L. *ChemPhysChem.* **2006**, *7*, 1086–1091.
(41) Gledison, S. F.; Giovanna, M.; Sergio, R.; Gerhard, H. F.; Jonder, M.; Maria, C. M. A.; Jairton, D. *J. Colloid Interface Sci.* **2006**, *301*, 193–204.
(42) Witkowska, A.; Dsoke, S.; Principi, E.; Marassi, R.; Cicco, A. D.; Albertini, V. R. *J. Power Sources* **2008**, *178*, 603–609.
(43) Ziegelbauer, J. M.; Olson, T. S.; Pylypenko, S.; Alamgir, F.; Jaye, C.; Atanassov, P.; Mukerjee, S. *J. Phys. Chem. C* **2008**, *112*, 8839–8849.
(44) Arruda, T. M.; Shyam, B.; Lawton, J. S.; Ramaswamy, N.; Budil, D. E.; Ramaker, D. E.; Mukerjee, S. *J. Phys. Chem. C* **2010**, *114*, 1028–1040.
(45) Mukerjee, S.; Srinivasan, S.; Soriaga, M. P.; McBreen, J. *J. Electrochem. Soc.* **1995**, *142*, 1409–1422.
(46) Sasaki, K.; Wang, J. X.; Naohara, H.; Marinkovic, N.; More, K.; Inada, H.; Adzic, R. R. *Electrochim. Acta* **2010**, *55*, 4331–4338.
(47) Zhang, J.; Vukmirovic, M. B.; Sasaki, K.; Nilekar, A. U.; Mavrikakis, M.; Adzic, R. R. *J. Am. Chem. Soc.* **2005**, *127*, 12480–12481.
(48) Fang, B.; Luo, J.; Chen, Y.; Wanjala, B. N.; Loukrakpam, R.; Hong, J.; Yin, J.; Hu, X.; Hu, P.; Zhong, C. J. *ChemCatChem* **2011**, *3*, 583–593.
(49) Gasteiger, H. A.; Kocha, S. S.; Sompalli, B.; Wagner, F. T. *Appl. Catal., B* **2005**, *56*, 9–35.
(50) Fang, B.; Wanjala, B. N.; Hu, X.; Last, J.; Loukrakpam, R.; Yin, J.; Luo, J.; Zhong, C. J. *J. Power Sources* **2011**, *196*, 659–665.